



Temperature and Melt Modeling on the Prince of Wales Ice Field, Canadian High Arctic

SHAWN J. MARSHALL

Department of Geography, University of Calgary, Calgary, Alberta, Canada

MARTIN J. SHARP

Earth and Atmospheric Sciences, University of Alberta, Edmonton, Alberta, Canada

(Manuscript received 7 April 2008, in final form 20 August 2008)

ABSTRACT

Near-surface temperature variability and net annual mass balance were monitored from May 2001 to April 2003 in a network of 25 sites on the Prince of Wales Ice Field, Ellesmere Island, Canada. The observational array spanned an area of 180 km by 120 km and ranged from 130 to 2010 m in altitude. Hourly, daily, and monthly average temperatures from the spatial array provide a record of mesoscale temperature variability on the ice field. The authors examine seasonal variations in the variance of monthly and daily temperature: free parameters in positive-degree-day melt models that are presently in use for modeling of glacier mass balance. An analysis of parameter space reveals that daily and seasonal temperature variability are suppressed in summer months (over a melting snow–ice surface), an effect that is important to include in melt modeling. In addition, average annual vertical gradients in near-surface temperature were $-3.7^{\circ}\text{C km}^{-1}$ in the 2-yr record, steepening to $-4.4^{\circ}\text{C km}^{-1}$ in the summer months. These gradients are less than the adiabatic lapse rates that are commonly adopted for extrapolation of sea level temperature to higher altitudes, with significant implications for modeling of snow and ice melt. Mass balance simulations for the ice field illustrate the sensitivity of melt models to different lapse rate and temperature parameterizations.

1. Introduction

Glacier and ice sheet models simulate glacier dynamics as a function of the bedrock topography, ice thickness, a constitutive relationship for ice rheology, and parameterizations of flow (i.e., sliding) at the base of the glacier. These models require detailed surface mass balance fields for simulations of glacier response to climate change: estimates of snow accumulation and snow/ice melt on scales of hundreds of meters to tens of kilometers, depending on the ice mass of interest. Mass balance modeling at a resolution of less than 10 km is needed to capture the gradients in topography and ice melt in the ablation zone of the Greenland Ice Sheet (Glover 1999; Box et al. 2006) and closer to 1 km for the mesoscale ice fields of the Arctic (e.g., Flowers et al. 2005).

The physics of snow and ice melt are well understood and can be accurately modeled given sufficient meteorological and snowpack data to describe the local energy balance (e.g., Cline 1997; Arnold et al. 1996). However, the meteorological data demands and the spatial variability of the governing processes make it difficult to apply a rigorous energy balance model in ice sheet–climate modeling. This is also true for paleoclimate studies and for regional-scale modeling studies, in which climatic fields need to be interpolated or downscaled to the region of interest (e.g., Radić and Hock 2006). In these situations, degree-day or “temperature index” models are commonly used to parameterize snow and ice melt as a function of air temperature (Reeh 1991; Braithwaite 1995).

Temperature-index models capitalize on the fact that air temperature is a strong indicator of net radiative and sensible heat energy available for melting (Ohmura 2001). These models are widely used for mass balance calculations in ice sheet studies (Letréguilly et al. 1991; Huybrechts et al. 1991; Pollard and Thompson 1997;

Corresponding author address: Shawn Marshall, Department of Geography, University of Calgary, 2500 University Dr. NW, Calgary, AB T2N 1N4, Canada.
E-mail: shawn.marshall@ucalgary.ca

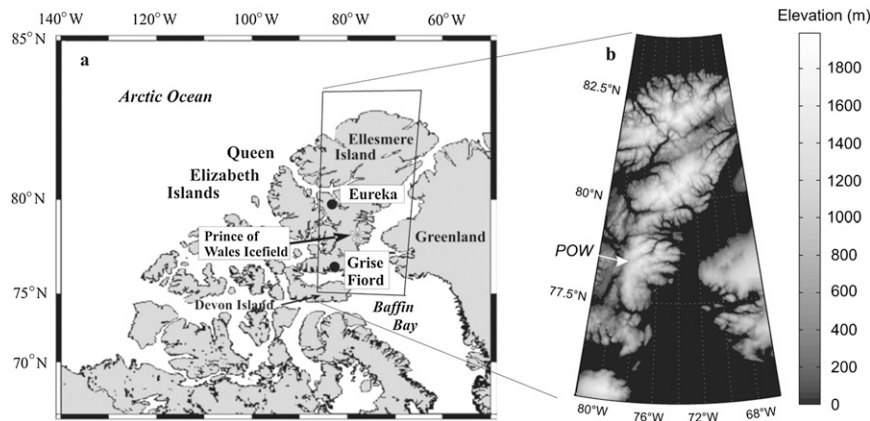


FIG. 1. (a) Location of the POW Ice Field and Meteorological Service of Canada monitoring sites in Eureka and Grise Fiord, Ellesmere Island, Nunavut, Canada. (b) Topography of Ellesmere Island and the POW Ice Field. Ice field geometry is shown in detail in Fig. 2.

Fabre et al. 1996; Huybrechts 2000; Hanna et al. 2005). Meltwater generated over time interval τ , $m(\tau)$, is estimated from

$$m(\tau) = f_{SI} \text{PDD}(\tau), \quad (1)$$

where f_{SI} is an empirically derived melt coefficient, distinct for snow (s) and ice (i), and $\text{PDD}(\tau)$ represents positive degree days, the integrated temperature above 0°C , over time interval τ ; that is,

$$\text{PDD}(\tau) = \int_0^\tau T(t)H(T)dt. \quad (2)$$

Here, $T(t)$ represents the near-surface atmospheric (screen) temperature at time t and $H(t)$ is a Heaviside function, equal to 1 when $T(t) \geq 0$ and equal to 0 when $T(t) < 0$.

PDD is a measure of the integrated heat energy in excess of the melting point over the time interval of interest. Melting is precluded with subzero temperatures. Snow and ice have distinct melt parameters to crudely parameterize the differences in albedo between the two surfaces. Melt coefficients f_{SI} have units of mm water equivalent (w.eq.) melt per ($^\circ\text{C}$ day), and are derived from field studies that relate measured ablation to near-surface (e.g., 2-m) screen temperatures (e.g., Braithwaite 1995; Bøggild et al. 1994; Jóhannesson et al. 1995). Braithwaite and Zhang (2000) give a summary of PDD factors that have been inferred from different sites.

Surface melt estimation from Eq. (1) is convenient because temperature is the only governing meteorological variable. If one has detailed temperature measurements from a site, PDD can be calculated directly through simple summation or integration of (2). Tem-

perature varies smoothly and linearly in space and time relative to meteorological variables such as wind conditions and cloud cover, making temperature amenable to spatial interpolation or extrapolation relative to other variables in energy balance calculations; therefore, $T(x,y,z,t)$ is more straightforward to predict from distant point observations or model predictions. Many studies have capitalized on this in extrapolating sea-level or low-altitude temperatures to higher elevations, typically through application of an atmospheric temperature lapse rate, $\beta_T = \partial T/\partial z$, which assumes that temperature decreases linearly with altitude in the lower troposphere.

In this paper we examine temperature variability and temperature, ablation, and mass balance gradients on the Prince of Wales (POW) Ice Field, Canadian High Arctic, based on 2 yr of net balance and temperature measurements across the ice field. Observations of temporal and spatial variations in temperature allow us to tune the parameterization of temperature in PDD melt models to optimize calculations of snow and ice melt over the ice field. Observation ablation and mass balance patterns are compared with mass balance models driven by regional weather observations from Eureka, Nunavut (Fig. 1a), the nearest available Environment Canada weather station (http://www.climate.weatheroffice.ec.gc.ca/climateData/canada_e.html). Eureka has a relatively complete set of long-term meteorological observations (1948–present), whereas other regional stations such as that at Grise Fiord have shorter records with numerous data gaps. Nevertheless, Eureka is 215 km from the summit site on the ice field and is at an elevation of 10 m, so there is a great deal of uncertainty in driving ice field mass balance from conditions in Eureka. This unfortunately reflects a typical reality in

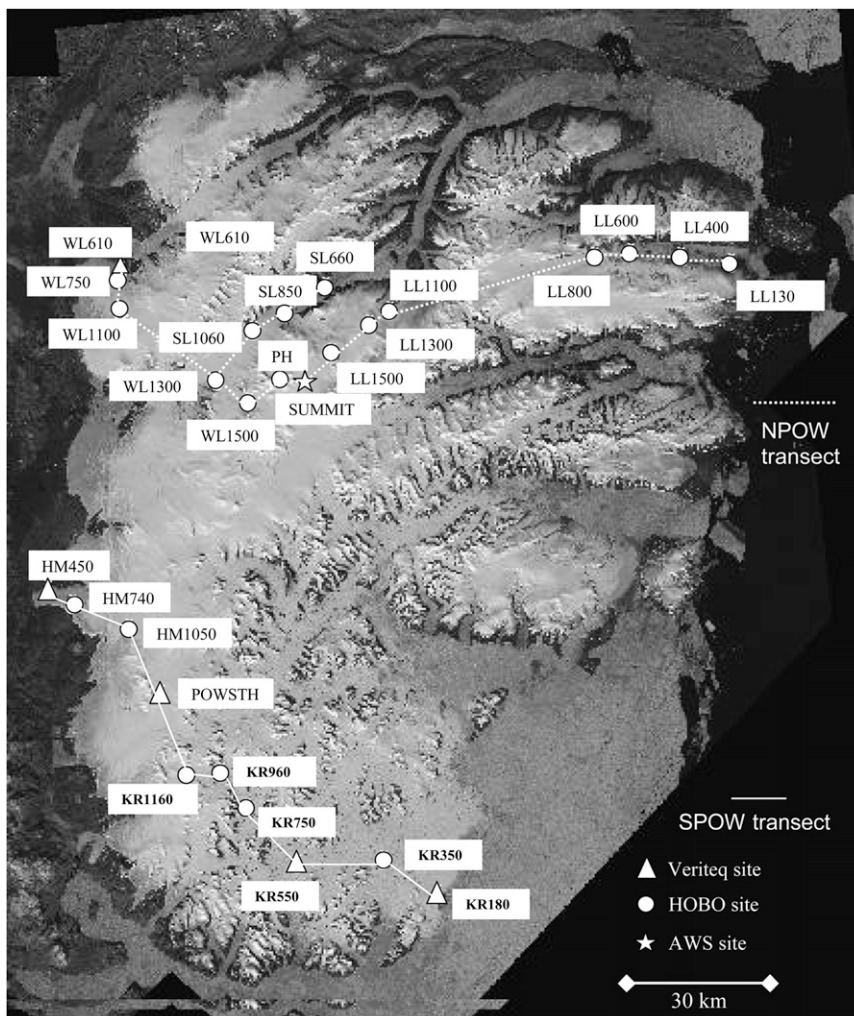


FIG. 2. Temperature monitoring sites on the POW Ice Field, 2001–03. The automatic weather station site is marked with a star, HOBO temperature datalogger sites are marked with circles, and Veriteq temperature–relative humidity monitoring sites are marked with triangles.

modeling of glacier mass balance; local weather records are seldom available, and extrapolation or downscaling strategies are needed to estimate ice field weather conditions from off-glacier site data or reanalyzed–modeled climate fields.

2. Field site

Air temperature, snow accumulation, and annual mass balance measurements were collected for the period May 2001 to April 2003 from a network of 25 sites on the Prince of Wales Ice Field, Ellesmere Island, Nunavut, Canada (Figs. 1 and 2). This high Arctic ice field has an area of 19 325 km², with a broad north-central plateau at an altitude of 1720 m. This plateau is the nominal ice divide, with nunataks extending above

the central plateau to elevations of more than 2000 m in several locations. The ice field descends to sea level on the east coast of Ellesmere Island and it terminates terrestrially on its western margin, at altitudes of 400 to 650 m. This asymmetry is due to a strong east–west gradient in the ice field’s snow accumulation regime, with southeasterly storm tracks from Baffin Bay providing the primary source of moisture for the ice field (Koerner 1979).

The observational network consists of two east–west lines crossing the ice field, one in the north (the NPOW line) and one in the south (the SPOW line). The NPOW line was established in May 2001 and is 166 km in length, with altitudes ranging from 130 m on the eastern margin to 2010 m at the highest point (Fig. 2). The NPOW line descends to 610 m on the terminus of an outlet lobe in

the west. The 131-km-long SPOW line was established in May 2002 and also descends to the ice margins on both the east and west sides of the ice field, with temperature monitoring sites at 180 m altitude on the eastern margin and 450 m in the west. The southern ice divide, the highest elevation of the SPOW line, has an elevation of 1350 m.

Temperature at each site was monitored at 30-min intervals using a combination of HOBO H8-PRO temperature loggers from Onset Scientific, Ltd., and SP2000 temperature-relative humidity loggers from Veriteq Instruments, Inc. Sensors were deployed in radiation shields and were mounted on 10-ft steel poles drilled into the ice. Hourly wind, radiation, snow depth, temperature, relative humidity, and air pressure data are also available for the period May 2001 to May 2003 from an automatic weather station (AWS) established on the interior plateau (1720-m altitude), although this dataset has gaps in the winter months due to loss of battery power. The AWS provides a complete record of snowfall–ablation on the ice field plateau for the summers of 2001 and 2002.

Snow samples from the 2002 and 2003 field seasons were collected from snow pits dug to the previous summer surface, demarcated by either glacial ice (at altitudes below the year's equilibrium line) or superimposed ice created by refrozen meltwater. This horizon, which cannot be penetrated with a shovel, represents the end of the previous melt season. It is typically assumed to date to around the end of August, although we can refine the chronology of the late-summer surface at each site using the local temperature data. Snow pits are dug during our field season from late April to mid-May, with any new snowfall during this time accounted for in the comparison. Bulk samples of fall, winter–spring, and recent snow were collected from each snow pit in 2002, with seasons distinguished based on snow type (hoar crystals in fall, dense wind-slab in winter–spring, and fresh powder constituting recent snowfall). In the 2003 season we sampled each snow pit at 10-cm intervals for the full depth of the pit, giving a continuous stratigraphy for snow density and stable isotope measurements.

3. Prince of Wales Ice Field mass balance, 2002/03

a. Snow accumulation

Snow accumulation patterns observed in the 2001–03 field seasons reflect those mapped by Koerner (1979), with eastern aspects averaging 1.8 times more snow-water-equivalent than the western aspects of the ice field. Snow accumulation data for different regions of

TABLE 1. POW Ice Field snow accumulation data, 2001–03. Snow depth d and snow-water equivalent SWE refer to the ca. 9-month winter accumulation, from the summer surface to the time of sampling (ca. September–May). Site data have been averaged to provide regional summaries.

Region	SWE (mm w.eq.)		d (cm)		ρ_s (kg m ⁻³)	
	01/02	02/03	01/02	02/03	01/0	02/03
NE flank	72	128	34	46	210	280
NW flank	60	94	24	30	250	310
North POW	70	120	30	44	230	280
SE flank	185	269	72	92	260	290
SW flank	100	111	31	32	320	350
South POW	153	215	56	69	270	310
East POW	129	193	53	67	240	290
West POW	76	101	26	31	290	330
Interior plateau	132	235	47	77	280	300
All sites	106	160	42	54	250	300
Ratios, all years						
E/W	1.7	1.9	2.0	2.2	0.84	0.88
NE/NW	1.2	1.4	1.4	1.5	0.84	0.89
SE/SW	1.9	2.4	2.4	2.9	0.79	0.83
S/N	2.2	1.8	1.9	1.6	1.17	1.13
SE/NW	3.1	2.9	3.1	3.0	1.01	0.94

the ice field are given in Table 1, based on snow pit depth and density measurements from May of 2002 and 2003 at the array of sites shown in Fig. 2. This reflects only the winter balance b_w : snow accumulation from the end of summer in the previous year to the time of visit (ca. September to May). We do not know summer snow accumulation totals from most of these sites. Summer snowfall totals in the interior plateau can exceed winter accumulation and may have a different spatial pattern than the winter snowpack. However, the basic pattern of aridification from southeast to northwest must hold for the annual accumulation, based on the asymmetry of the terminus altitudes.

b. Net mass balance

Net mass balance b_n for the balance year starting and ending in May can be determined from the change in stake heights at each site. Snow depth and density measurements are used to convert this to water equivalence. Where a portion of the stake-height change is due to ice melt, we assume that ice has a constant density of 900 kg m⁻³. Table 2 compiles temperature and mass balance data for the 2002/03 balance year, for which we have a more complete record over the ice field. We do not have temperature and net balance data from some sites (e.g., LL130, KR180) because poles melted out. Batteries failed in the temperature loggers at other locations. Overall, 22 of our instrumented sites have complete mass balance data for 2002/03, with summer

TABLE 2. POW Ice Field temperature and mass balance data, 2002/03; T_{\min} and T_{\max} are the minimum and maximum daily average temperatures, \bar{T}_a is the average annual temperature, PDD denotes the positive degree days measured at each site, N_m is the number of days with temperatures exceeding 0°C , and b_w , b_s , and b_n refer to the winter (\sim September–May), summer (\sim JJA), and net annual mass balance for the balance year June 2002–May 2003.

Site	T_{\min} ($^\circ\text{C}$)	T_{\max} ($^\circ\text{C}$)	\bar{T}_a ($^\circ\text{C}$)	PDD ($^\circ\text{C day}$)	N_m (days)	b_w	b_s	b_n
						(mm w.eq.)		
North Transect								
LL130		5.76		127	99	15		
LL400	−34.89	4.80	−13.84	112	100	113	−1059	−946
LL600	−37.92	3.52	−15.23	80	89	103	−480	−377
LL800						108	−254	−146
LL1100	−42.45	3.03	−18.40	28	55	170	−5	165
LL1300	−41.80	1.54	−18.41	13	36	136	63	199
LL1500	−44.31	0.69	−20.90	3	20	252	93	345
POWN		−0.98		1	12	215	138	353
POWHI	−37.75	−2.30	−19.07	0	2	132	63	195
WL1300	−39.30	3.75	−18.63	11	20	150	53	203
WL1100	−38.55	1.74	−17.33	22	54	74	0	74
SL1060						189	−2	187
SL850	−43.01	4.47	−18.23	44	65	123	−134	−11
WL750	−38.27	4.83	−15.	07	82	20	−527	−507
WL610	−41.91	6.78	−15.72	213	92	5	−965	−960
South Transect								
KR350		2.50		50	80	268	−525	−257
KR550	−41.62	2.89	−17.15	54	81	293	−109	184
KR750		2.97		54	75	217	−71	146
KR950	−41.27	3.17	−17.39	33	52	243	−7	236
POWS	−42.94	0.71	−20.55	7	22	303	94	397
HM1050	−40.28	2.67	−17.75	15	43	91	36	127
HM750		2.51		48	63	81	−156	−75
HM450	−41.73	5.66	−15.19	167	96	0	−1031	−1031

temperature data from 21 locations and 16 sites with complete annual temperature records. An additional source of error arises in the stake method for mass balance in the accumulation area because some meltwater percolates into the snowpack and refreezes internally, producing an apparent surface drawdown without a loss of mass.

c. Melt patterns

We do not have direct observations of summer snow–ice melt over the ice field, but net balance and winter (September to May) snowpack data can be combined to quantify net summer balance at each site: $b_s = b_n - b_w$. This is also compiled in Table 2. This provides some indication of the extent of summer melting at each site but is confounded by summer snowfall and internal accumulation due to refreezing of percolating meltwater—hence the positive balance at high-elevation sites in summer 2002. In summer [June–August (JJA)] 2002 there was no melting at the AWS site, but there was 55 cm of snow accumulation (138 mm w.eq.). Just over 1000 mm of melt occurred on both the western and eastern margins of the ice field.

d. Temperature characteristics

The temperature data are discussed in detail in Marshall et al. (2007) and summary statistics are presented in Table 2. The array of temperature dataloggers enables calculation of the number of melt days and total positive degree days PDD at each site (Table 2), providing an indirect proxy for snow–ice melt energy. PDD totals correlate well with stake and snow pit estimates of the summer mass balance ($r = -0.92$), indicating that PDD provide a good indication of melt energy. Net balance b_n is also strongly correlated with PDD ($r = -0.93$). This is consistent with the assertion of Koerner (2002) that summer melting dominates the annual mass balance in the Canadian high Arctic, even in this year of high accumulation totals and positive overall mass balance.

Figure 3 plots the relationship between annual PDD totals, melt days, and summer mass balance b_s for all sites on the ice field. PDD totals increase nonlinearly with melt-day totals (Fig. 3a). Summer mass balance also scales nonlinearly with melt days (Fig. 3b). An exponential or polynomial fit to the data could provide a reasonable predictive relationship between the two

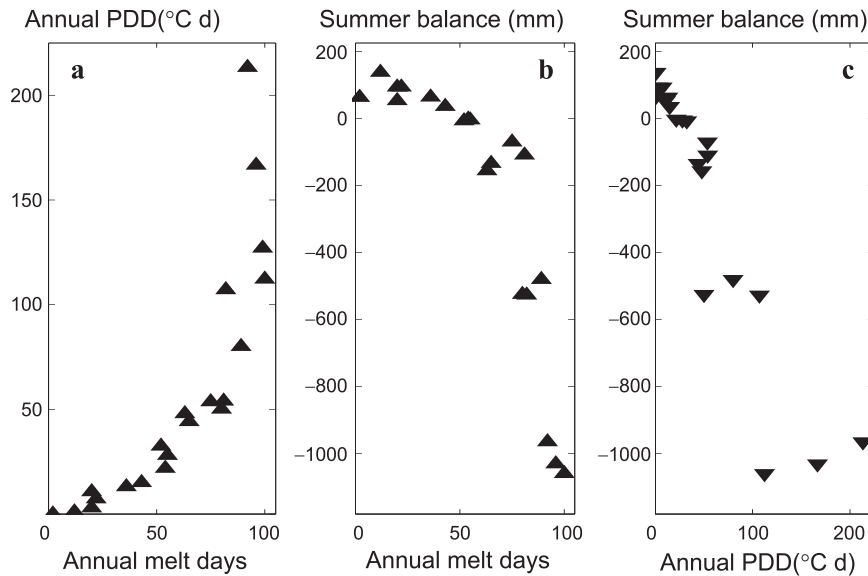


FIG. 3. Relationships between annual positive degree days, melt days, and summer mass balance b_S , 2002/03 balance year: (a) annual PDD vs melt days, (b) summer balance vs melt days, and (c) summer balance vs annual PDD. In these plots and throughout the manuscript, the ordinate is labeled horizontally and above the plot.

fields. This is of interest because melt-day totals can be accurately assessed from satellite microwave imagery (Wang et al. 2005, 2007), but the quantitative relationship with glacier mass balance is uncertain. Summer melting scales more linearly with PDD totals (Fig. 3c), although there is considerable scatter at the warmest sites. Two of these locations are on the western margin, WL610 and HM450. These sites are adjacent to low-albedo bedrock and soil surfaces in the summer months, providing an effective local source of longwave and sensible heat fluxes that contribute to the high PDD totals.

4. Temperature and melt modeling

In general, detailed knowledge of meteorological conditions is unavailable on a glacier or ice field, and positive degree days or the terms in a more rigorous energy balance must be modeled for a region. We restrict our attention to degree-day melt modeling here. This requires a number of characteristics of temperature variability to be characterized for a region. For large-scale hydrological or glacier mass balance modeling, either monthly or mean annual temperatures are generally used to estimate snow and ice melt through temperature-index models. We consider both annual and monthly PDD methods, with the aim of assessing which temperature parameterizations give the best representation of observed PDD totals on the ice field.

a. Annual and monthly degree-day methods

Reeh (1991) has developed a compact parameterization of daily average temperature T_d within the context of a simplified sinusoidal annual temperature cycle:

$$T_d(t) = \bar{T}_a - A \cos[2\pi(t - \phi)/\tau], \quad (3)$$

where \bar{T}_a is mean annual temperature, t is time in days, ϕ is a time lag, and τ is the length of the year (365.24 days). This assumes an annual temperature cycle with a half-amplitude $A = T_{\max} - \bar{T}_a$, where T_{\max} is the maximum summer temperature. Time $t = 0$ is taken as January 1, with ϕ introducing a time lag to describe heat capacity effects (seasonal thermal inertia). The latter is rarely introduced because Eq. (3) can be integrated over the length of the year τ to give cumulative annual PDD, the parameter of broad interest for glacier mass balance modeling. If only annually integrated values are needed, ϕ has no effect.

To provide a representation of temperature variability due to both diurnal cycles and synoptic variability, Reeh (1991) treats daily temperature T_d as a normally distributed variable, with standard deviation σ_d . Net annual PDD are then calculated from

$$\text{PDD}_a = \frac{1}{\sigma_d \sqrt{2\pi}} \int_0^\infty T \left\{ \int_0^\tau \exp[-(T - T_d)^2 / (2\sigma_d^2)] dt \right\} dT, \quad (4)$$

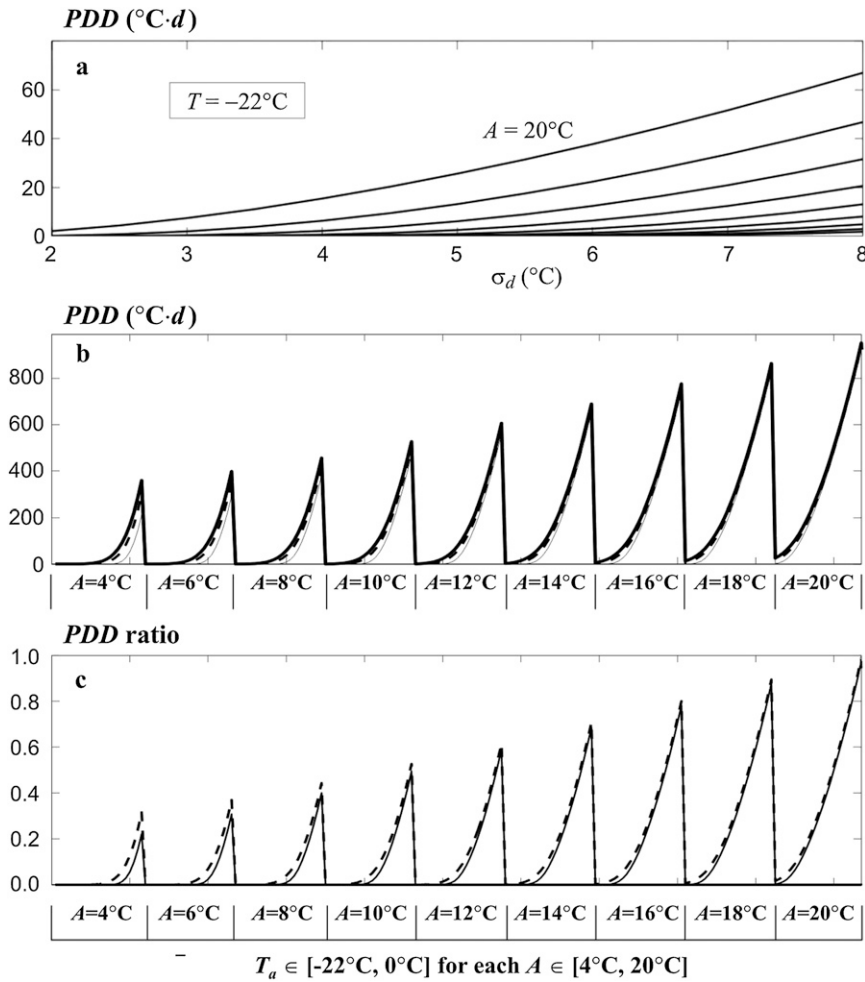


FIG. 4. (a) Annual PDDs calculated as a function of the standard deviation in daily temperature in Eq. (3). The family of curves corresponds to a mean annual temperature of -22°C and half-amplitudes of the annual cycle, $A \in [4, 20]^\circ\text{C}$, increasing upward. (b), (c) Alternative cross sections through this parameter space. (b) Annual PDD totals for mean annual temperatures $T_a \in [-22, 0]^\circ\text{C}$ for $\sigma_d = 2^\circ\text{C}$ (thin solid line), $\sigma_d = 4^\circ\text{C}$ (dashed line), and $\sigma_d = 5^\circ\text{C}$ (thick solid line). The panels correspond to half-amplitudes of the annual cycle, $A \in [4, 20]^\circ\text{C}$. (c) The ratio of annual PDDs for $\sigma_d = 4^\circ\text{C}/\sigma_d = 5^\circ\text{C}$ (dashed line) and $\sigma_d = 2^\circ\text{C}/\sigma_d = 5^\circ\text{C}$ (solid line).

where T_d is taken from Eq. (3). Equation (4) is numerically integrated over the year and the range of positive temperatures $T \in [0, \infty]$. In this formulation, σ_d is primarily representative of the standard deviation of the daily temperature cycle (the diurnal range), although synoptic variability can also introduce large deviations from the mean daily temperature of a simple sinusoid; σ_d in (4), or as measured in actual temperature data, includes all factors that cause temperature to deviate from the idealized sinusoid, including both diurnal and synoptic variability.

As an alternative to sinusoidal representation of the annual cycle, net monthly PDD can be calculated from monthly mean temperatures \bar{T}_m and a measure of

the standard deviation in monthly temperatures, σ_m (Braithwaite and Olesen 1989; Braithwaite 1995):

$$\text{PDD}_m = \frac{\tau_m}{\sigma_m \sqrt{2\pi}} \int_0^\infty T \exp[-(T - \bar{T}_m)^2 / (2\sigma_m^2)] dT, \quad (5)$$

where τ_m is the length of the month. The parameter σ_m differs from σ_d in Eq. (4) in that it now represents the net variability around monthly mean temperatures, associated with seasonal transitions as well as diurnal and synoptic variability.

In degree-day melt modeling, monthly or annual PDD are used to estimate monthly or net annual melt from

Eq. (1). The appropriate choice of standard deviation values in degree-day melt modeling, σ_d and σ_m , has not been widely discussed. Lefebre et al. (2002) simulate this parameter in regional climate modeling of screen temperatures over the Greenland Ice Sheet and note its potential importance in melt modeling. No distinction is generally made between daily and monthly standard deviations. Values of $\sigma_d = 2.5^\circ\text{C}$ and $\sigma_m = 4^\circ$ to 5°C are commonly used in glacier modeling. The integrated PDD heat energy that is available for melt is sensitive to this parameter, however. Figure 4a plots solutions to the annual PDD integral of Eq. (4) for a range of standard deviations $\sigma_d \in [2^\circ\text{C}, 8^\circ\text{C}]$ and annual cycle half-amplitudes $A \in [4^\circ\text{C}, 20^\circ\text{C}]$ for a mean annual temperature of $\bar{T}_a = -22^\circ\text{C}$. These values for mean annual air temperature and the annual temperature range give daily average summer temperatures that are below the melting point for the entire range of tests, similar to conditions in the interior of the POW Ice Field. However, daily temperature variability gives positive PDD totals, increasing with σ_d and A . High values of σ_d and A also increase the number of days per year with temperatures exceeding 0°C .

Figures 4b and 4c offer an alternative cross section of this phase space. Figure 4b plots annual PDD totals for a suite of mean annual temperatures $\bar{T}_a \in [-22^\circ\text{C}, 0^\circ\text{C}]$ and half-amplitude values $A \in [4^\circ\text{C}, 20^\circ\text{C}]$ for $\sigma_d = 2^\circ, 4^\circ$, and 5°C . The ratios PDD ($\sigma_d = 2$)/PDD ($\sigma_d = 5$) and PDD ($\sigma_d = 4$)/PDD ($\sigma_d = 5$) for each (\bar{T}_a, A) pair are plotted in Fig. 4c, illustrating the significantly reduced PDD total (hence, available melt energy) with reduced temperature variability. The ratio for the $\sigma_d = 2^\circ\text{C}$ and $\sigma_d = 5^\circ\text{C}$ cases has a mean of 0.45 for the range of tests, indicating a 55% reduction in available melt energy for the low-variability case, on average. PDD ratios in cases ($\sigma_d = 4^\circ\text{C}$)/($\sigma_d = 5^\circ\text{C}$) have a mean value of 0.67.

These considerations apply to the pure PDD approach to melt modeling. As an intermediate approximation to a full energy balance, Cazorzi and Dalla Fontana (1996) and Hock (1999) have extended temperature-index models to include a term for potential solar radiation, which can be theoretically calculated for a site. Mixed temperature and radiation melt models are more physically based, allowing a direct means of including the effects of changing surface albedo, for instance. However, they still rely on parameterizations of temperature and PDD, so the analyses considered here apply equally to this class of melt models.

b. Observed temperature variability

Table 3 summarizes the observed daily and monthly standard deviations at each site for 2002/03, as well as monthly near-surface temperature lapse rates on the ice

TABLE 3. Average temperature variance and near-surface temperature lapse rates calculated from hourly data for all available stations, 2002/03; r_{Tz} and $r_{\sigma z}$ are linear correlations with altitude for the monthly, seasonal, and annual mean and standard deviation of temperature.

Period	$\bar{\sigma}_m$ ($^\circ\text{C}$)	$\bar{\sigma}_d$ ($^\circ\text{C}$)	$\overline{dT/dz}$ ($^\circ\text{C km}^{-1}$)	r_{Tz}	$r_{\sigma z}$
May	5.25	2.14	-3.1	-0.89	0.10
June	3.10	1.35	-5.4	-0.97	0.71
July	2.34	1.19	-5.1	-0.95	0.80
August	2.45	1.29	-4.6	-0.92	0.70
September	3.89	1.80	-4.8	-0.86	-0.06
October	6.45	2.04	-4.3	-0.80	0.31
November	5.25	2.13	-3.0	-0.58	-0.38
December	6.92	2.21	-3.6	-0.78	-0.57
January	5.76	2.04	-3.3	-0.58	-0.01
February	4.10	1.87	-1.1	-0.23	-0.19
March	5.56	1.95	-0.7	-0.08	-0.37
April	4.67	2.37	-2.5	-0.55	0.06
Summer (JJA)	2.63	1.27	-5.1	-0.96	0.80
Fall (SON)	5.20	1.99	-4.1	-0.82	0.04
Winter (DJF)	5.60	2.05	-2.7	-0.56	-0.33
Spring (MAM)	5.16	2.15	-2.1	-0.58	-0.20
Mean annual	4.65	1.86	-3.6	-0.83	0.13

field. Here σ_d and σ_m are calculated from daily and monthly compilations of the 30-min temperature observations and have the same meaning as in Eqs. (4) and (5). Monthly and daily variability both exhibit a strong seasonal cycle, with reduced variability during summer months. The explanation is simple; temperature is locked in at 0°C on a melting snow-ice surface, unable to warm above that and with latent heat release from refreezing meltwater suppressing the magnitude of cooling during cold periods during the melt season. This keeps the surface temperature near 0°C and it dampens near-surface temperature variability, relative to the diurnal and synoptic weather-induced variability that characterizes near-surface boundary layer temperatures over subzero snow and ice surfaces.

This summer reduction in monthly and daily temperature variability means that annual average values of σ_m and σ_d are not representative of melt-season conditions. The lower values observed in summer months are more appropriate for PDD-based melt modeling. It may also be worthwhile to introduce spatially (altitudinally) varying values of σ_m and σ_d to account for the generally higher values found at high elevations in summer months (Table 3), where nonmelting conditions are more prevalent. There is no significant variation with altitude in other seasons.

Near-surface temperature lapse rates also have a seasonal cycle, with steeper gradients in the summer and more persistent inversions giving weak temperature gradients in the winter months. The lapse rate variability

summarized in Table 3 has been discussed in detail elsewhere (Marshall et al. 2007). Overall, a melt-season lapse rate of $\beta_T = -4.5^\circ\text{C km}^{-1}$ gives the best fit to the temperature data at the site over the 2-yr record, with synoptically governed daily and interannual variability.

5. POW Ice Field temperature and PDD modeling

The POW temperature dataset provides a set of observations that can be used to optimize degree-day melt models for this region. We evaluated several different PDD parameterizations, including the introduction of seasonal cycles in daily and monthly standard deviation of temperature to reflect the lower amount of variability in summer months (over a melting glacier surface). Modeled annual PDD and melt days can be compared with observations for each case.

Three different models were explored for monthly PDD modeling, using measured monthly temperature values for each site: (i) variable monthly standard deviation of temperature σ_m , based on the actual data at each site, (ii) fixed σ_m , and (iii) a sinusoidal annual cycle for σ_m , based on a mean annual value $\bar{\sigma}_m$ and annual amplitude $A_{\sigma m}$:

$$\sigma_m = \bar{\sigma}_m + A_{\sigma m} \cos\left(\frac{2\pi t}{\tau}\right), \quad (6)$$

where τ is the length of the year and $t = 0$ on January 1.

The first case gives the best fit to the observations, naturally, but is impractical for temperature and melt modeling because one usually does not know the actual conditions at a site. We searched parameter space for optimal values of σ_m for the fixed case and the annual cycle, with goodness-of-fit evaluated by the rms misfit to the observed annual PDD total at each site. For fixed values of σ_m the best results were found for $\sigma_m = 2.4^\circ\text{C}$, considerably less than the observed mean annual value in our data, $\bar{\sigma}_m = 4.26^\circ\text{C}$. The lower value is favored because summer standard deviations are low and summer is the crucial time for melting. Building the seasonal cycle into σ_m gives a slightly improved fit to the observations, with the best results found for $\bar{\sigma}_m = 4.2^\circ\text{C}$ and an annual amplitude $A_{\sigma m} = 2.0^\circ\text{C}$. This is close to the mean value of observations from all sites, $A_{\sigma m} = 2.3^\circ\text{C}$.

Table 4 summarizes the PDD models that we explored and the parameter settings that give the closest fit to the data in each case. The results for each site are plotted in Fig. 5a. The parameterization with the annual σ_m cycle is our preferred model for PDD-based melt modeling based on monthly temperatures.

A similar sensitivity study was done for annual PDD functions, which may be more appropriate if monthly temperature data are unavailable. The annual method

TABLE 4. Fits to the data for monthly and annual PDD models.

Case	Optimal parameter settings		RMS misfit ($^\circ\text{C day}$)
	σ_m ($^\circ\text{C}$)	$A_{\sigma m}$ ($^\circ\text{C}$)	
Monthly PDD model			
Local monthly values of σ_m	Variable	n/a	7.1
Fixed σ_m	4.5	0	54.4
Fixed σ_m	2.4	0	10.7
Annual σ_m cycle	4.2	2.0	10.4
Annual PDD model			
Local daily values of σ_d	Variable	n/a	$T_{\text{July}} - \bar{T}_a$ 64.0
Fixed σ_d	6.2	n/a	$T_{\text{July}} - \bar{T}_a$ 31.2
Local daily values of σ_d	Variable	n/a	$T_{\text{max}} - \bar{T}_a$ 26.2
Fixed σ_d	0.5	n/a	$T_{\text{max}} - \bar{T}_a$ 23.2
Annual σ_d cycle	1.8	0.6	$T_{\text{max}} - \bar{T}_a$ 32.5

requires knowledge of the mean annual temperature \bar{T}_a and the amplitude of the annual cycle A_T , with the latter often prescribed from the difference between mean July temperatures and \bar{T}_a . The standard deviation of daily temperatures σ_d is then the only free parameter in the annual temperature model. The mean summer value of this parameter is $\bar{\sigma}_d = 1.27^\circ\text{C}$.

Unlike the results with the monthly method, the best fit to the observed annual PDD is not attained with the actual local values of \bar{T}_a , A_T , and σ_d (Table 4). Mean July temperatures give too low an annual temperature range, 15.9°C on average, which leads to cool summer temperatures and a bias to low modeled PDD totals. With this method of calculating A_T , the best fit to the data corresponds to the setting $\sigma_d = 6.2^\circ\text{C}$. We find better results with A_T calculated from the warmest day of the year, rather than mean July temperatures. In this case, the average value of A_T is 20.5°C and the best fit to the data corresponds with $\sigma_d = 0.5^\circ\text{C}$. Modeled melt statistics for these two cases are plotted in Fig. 5c. We also investigated a sinusoidal annual cycle for σ_d , again reflecting the reduced variability during summer months, but found no improvement over the full-amplitude, low-variability model with constant σ_d .

We could not find parameter settings with a sinusoidal annual temperature cycle that gave as strong a result as with the monthly PDD method. Figure 6 illustrates the reason for this for the two A_T treatments. Monthly mean temperatures provide a closer fit to the actual temperature data, with the idealized sinusoid providing a reasonable but more approximate representation. When temperatures are close to the threshold for melting, short periods of warmer-than-average synoptic weather conditions are very important to annual PDD

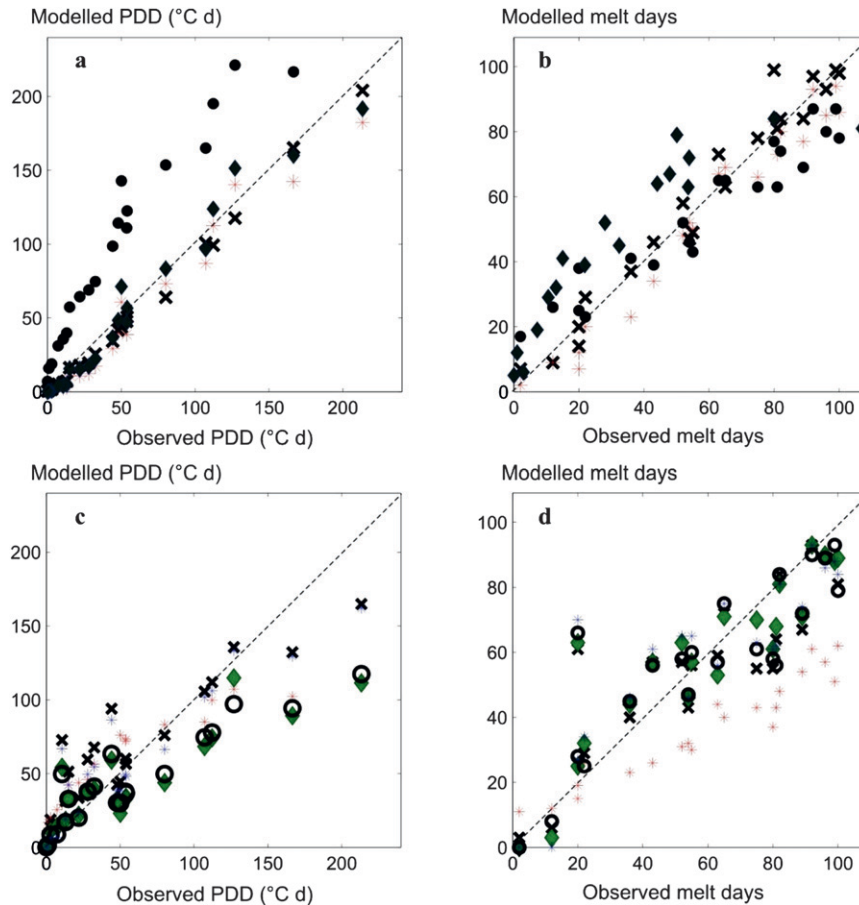


FIG. 5. Modeled vs observed (a),(c) PDD totals and (b),(d) melt days for all sites on the ice field for the 2002/03 balance year. (a),(b) Monthly PDD modeling, for the reference case with local monthly values of σ_m (\times symbols), for $\sigma_m = 4.2^\circ\text{C}$ (black filled circles) and 2.4°C (stars), and with an annual σ_m cycle (diamonds). (c),(d) Annual PDD modeling, with $A_T = T_{\max} - T_a$ unless stated otherwise: reference case with local values of σ_d (\times symbols); $\sigma_d = 0.5^\circ\text{C}$ (blue stars) and 6.2°C with $A_T = T_{\text{July}} - \bar{T}_a$ (red stars); a site-specific annual σ_d cycle (diamonds); and a fixed annual σ_d cycle (black open circles).

totals and are better captured by the monthly mean temperatures than the annual sinusoid.

6. Mass balance modeling

Figure 7a plots simulated positive degree days for 2002/03 on the POW Ice Field, based on the optimized temperature model and meteorological data from Eureka. We use variable near-surface lapse rates with a mean summer value of -5°C km^{-1} to project monthly temperature from Eureka to the ice field, based on observations from the 2002/03 balance year (Table 3), presented in detail in Marshall et al. (2007). A seasonal temperature offset is also applied in projecting temperatures from Eureka to the ice field, based on observations that indicate warmer summer conditions and colder winter conditions in Eureka. This offset is pre-

sumably a result of the regional cooling effect of the ice field and the high continentality of the Eureka site.

Figure 7b plots modeled 2002/03 mass balance for this scenario. This provides an illustration of the mass balance regime of the ice field in a positive mass balance year such as 2002/03, but it is not a credible simulation because we have an overly simplified model of ice field precipitation. Site precipitation P_s is parameterized following $P_s = \beta_P z_s P_E$, where P_E is the monthly precipitation in Eureka, z_s is the site elevation, and β_P is a factor that gives annual snow accumulation totals at the summit site that match the 2002/03 observations (2.5 times the precipitation total in Eureka). This is an expedient way to parameterize the orographic enhancement of precipitation on the ice field, but it does not capture the strong southeast–northwest regional precipitation gradient on the POW Ice Field. Mass

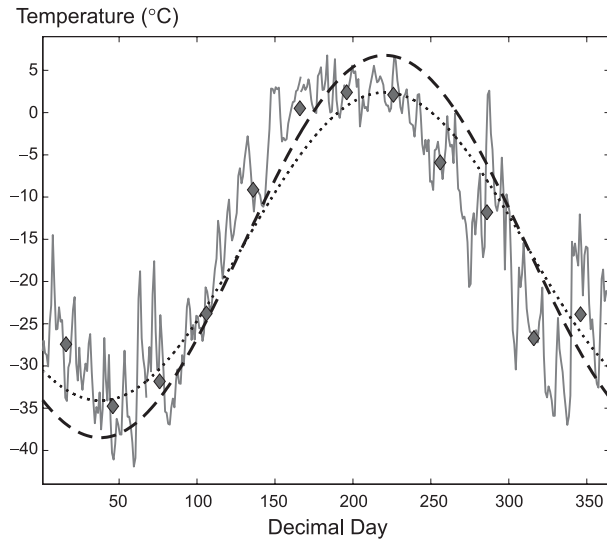


FIG. 6. Illustration of the observed vs modeled annual temperature cycle for site WL610 on the western flank of the ice field. Measured mean daily temperature (gray line), mean monthly temperature (diamonds), and modeled annual cycle with $A_T = T_{\max} - \bar{T}_a$ (solid black line) and $A_T = T_{\text{July}} - \bar{T}_a$ (dashed black line). A 40-day phase lag is used in the modeled cycle.

balance modeling efforts in this region need to parameterize this pattern or include physically based precipitation models (e.g., Purves and Hulton 2000; Smith and Barstad 2004).

To illustrate the sensitivity of modeled mass balance to the choice of lapse rate, Fig. 8 plots average annual PDD for the period 1948–2006, based on average monthly climatology in Eureka. Temperature and precipitation have been upscaled to the ice field as in Fig. 7 but for three different summer lapse rates: $\beta_T = -4^\circ$, -6° , and -8° km^{-1} . Figure 8d plots the difference in

average annual mass balance for the warm versus cold scenarios on the ice field, $\beta_T = -4^\circ \text{ km}^{-1}$ minus $\beta_T = -8^\circ \text{ km}^{-1}$. The equilibrium line, where accumulation equals melt, is superimposed for each of these cases in Fig. 8d. The choice of lapse rate is clearly crucial to mass balance modeling, primarily through its influence on PDD totals. The choice depicted in Fig. 8c, $\beta_T = -8^\circ \text{ km}^{-1}$, is commonly adopted in high latitudes because it is typical of adiabatic lapse rates in a relatively dry atmosphere. Observed temperature and mass balance data suggest that this choice is inappropriate and leads to severe underestimation of modeled snow–ice melt, at least for this region.

Modeled and observed PDD and annual mass balance are shown in Fig. 9 for several different summer-season lapse rates. West-to-east cross sections are plotted separately for the north and south transects. This plot illuminates the importance of the assumed lapse rate, as well as several shortcomings in the mass balance model. The simulation with $\beta_T = -5^\circ \text{ km}^{-1}$ gives a good fit to observed PDD in interior regions of the ice field, but PDD and melt are underestimated on the western flanks of the ice field and overestimated at the lowest elevations in the east. This may be a consequence of local continental and marine influences at these marginal sites. The western margins experience warm air advection from the adjacent land, whereas fog and cloud cover on the east coast reduce summer temperatures and lower PDD relative to the model. The climate forcing is a simple temperature extrapolation that neglects these meteorological influences. The PDD model is likely inappropriate to this site. We use literature values for the melt factors, derived from Greenland (Braithwaite and Olesen 1989), and have made no attempt to tune the PDD melt factors specifically for the ice field.

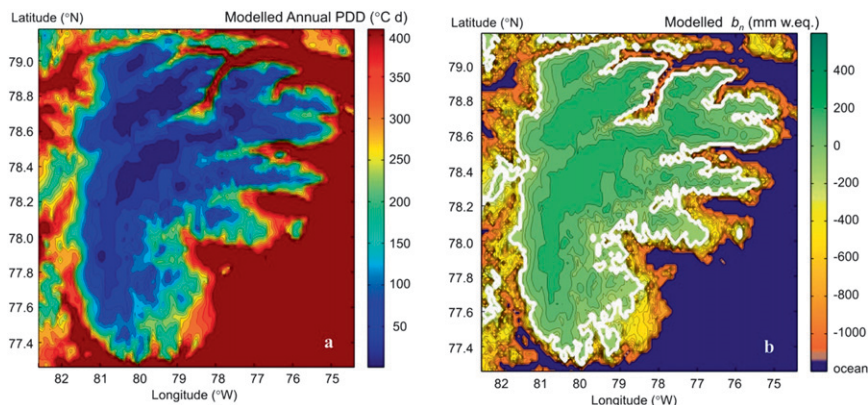


FIG. 7. Modeled PDD and mass balance on the POW Ice Field, 2002/03. (a) Annual PDD, contour interval of 20°C day . (b) Net annual mass balance, contour interval of 100 mm w.eq. The white line indicates the equilibrium line, where $b_n = 0$ (accumulation equals melt).

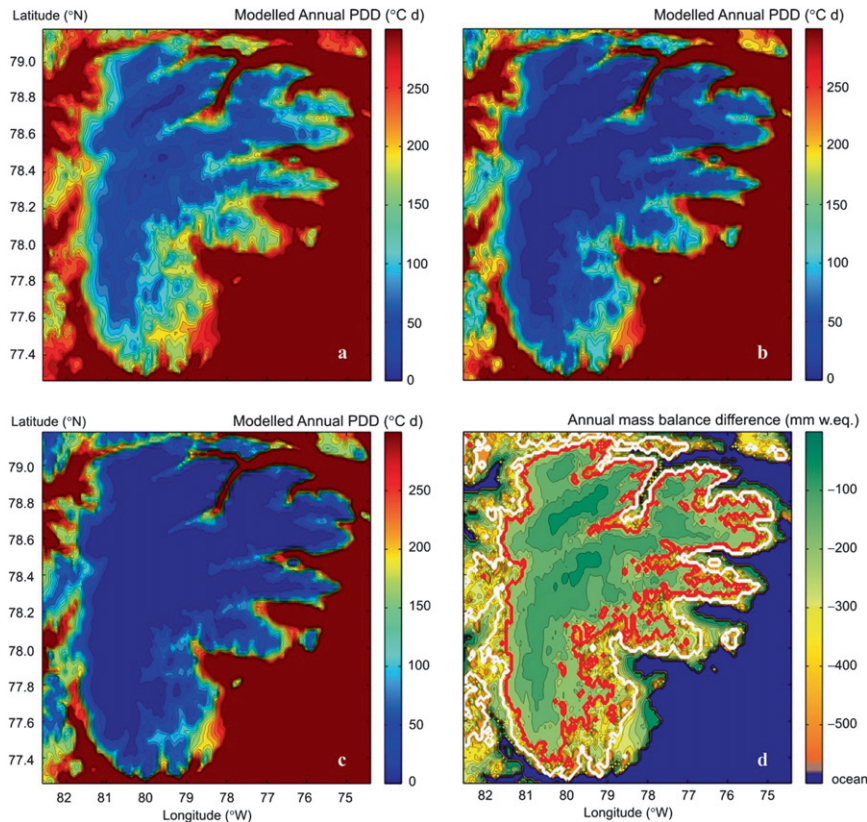


FIG. 8. Modeled annual PDD on the POW Ice Field based on average monthly temperatures in Eureka, Nunavut, 1948–2006, scaled to the ice field under different temperature lapse rates: (a) -4° , (b) -6° , and (c) $-8^{\circ}\text{C km}^{-1}$. Contour interval is 20°C day . (d) The difference in modeled mass balance for case (a) minus case (c), with a contour interval of 50 mm . The white and red lines indicates the equilibrium lines for $\beta_T = -8^{\circ}$ and $-4^{\circ}\text{C km}^{-1}$, respectively.

Such a tuning is likely unwarranted. Given the complex spatial gradients in elevation and continentality for this ice field, weaknesses of the melt model are likely due to the neglect of governing energy balance processes such as variations in cloud cover, sensible heat flux from Baffin Bay and the western terrestrial margins, and surface albedo fluctuations associated with summer snowfall and variable melt patterns. The shortcomings of the melt model are dominated by errors in the temperature modeling, not the PDD approach itself.

Some of the problems associated with a uniform temperature extrapolation (single lapse rate) are illustrated in Fig. 10, which plots the “ideal” local lapse rate that is needed to map temperatures from the Summit site to all other sites on the ice field. Assuming that temperatures are accurately known or modeled at one point on the ice field, these are the local, site-specific lapse rates that would be needed for accurate modeling of 2002/03 temperatures. Winter inversions give consistently shallower lapse rates for annual temperatures (circles), relative to the summer season (crosses). There

is considerable intersite variability, but the most systematic pattern that emerges reflects the observed PDD and mass balance patterns in Fig. 9: steeper summer lapse rates, indicating warmer low-elevation temperatures, on the western margins.

Another discrepancy in our mass balance modeling is associated with the simplicity of our uniform mapping of precipitation. Errors in modeled accumulation and net annual mass balance reflect the lack of a regional (southeast–northwest) precipitation gradient in our model (cf. Table 1). Net annual balance is well predicted in the north, with the exception of the western margin where melt is underestimated, but modeled mass balance is too low for the southeastern sector of the ice field. Modeled PDD are reasonable here so this is likely due to underprediction of annual accumulation. This is consistent with the observed high rates of snow accumulation in this quadrant of the ice sheet. We could specify an empirical distribution of precipitation over the ice field to improve the simulation, but a physically based model would be preferable because our empirical

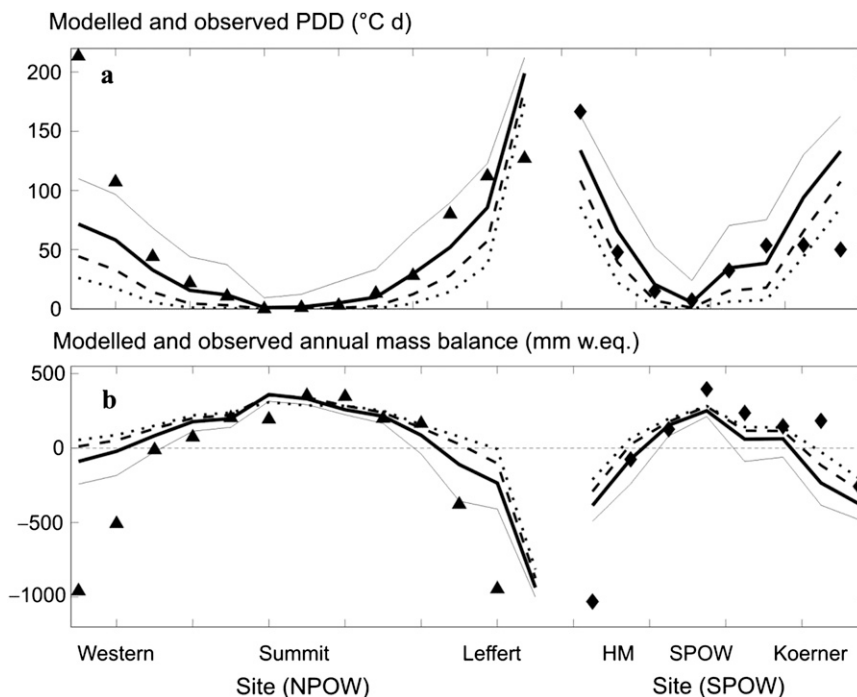


FIG. 9. Modeled (a) PDD and (b) annual mass balance under different lapse rate scenarios for POW Ice Field monitoring sites. (left side) NPOW transect sites (triangles), from west to east; (right side) SPOW transect sites (diamonds). Lines show for modeled PDD and b_n for $\beta_T = -3.5^\circ$ (thin solid line), -5° (thick solid line), -6.5° (dashed line), and $-8^\circ \text{C km}^{-1}$ (dotted line).

dataset is limited and may not reflect a “normal” year. We also lack data on summer snow accumulation patterns on the ice field; although available observations from the summit site indicate that this can be a substantial fraction of total annual accumulation ($\sim 50\%$).

Observations of net annual accumulation over the ice field are needed to properly evaluate mass balance simulations such as that of Fig. 9. Because of the large spatial gradients in snowfall in this region, our simple treatment of precipitation gives local errors of up to $100 \text{ mm w.eq. yr}^{-1}$ in the modeled mass balance, which are less than the error associated with melt modeling at the ice margins (in excess of $500 \text{ mm w.eq. yr}^{-1}$) but which can be systematic and cumulative over a large area of the ice field. Mass balance modeling efforts for the Canadian Arctic ice fields require a more sophisticated treatment of precipitation patterns, with independent means of evaluating modeled accumulation and melt.

7. Conclusions

A network of meteorological monitoring sites provides a detailed 2-yr record of regional temperature patterns across a high Arctic ice field. This dataset offers insight into the relationship between positive-degree-day totals (a proxy for melt energy) and the number of melt

days on the ice field, which is a variable that can be remotely monitored over large spatial scales. It may be possible to exploit this relationship to improve the quantitative skill of remote sensing-derived estimates of glacier mass balance.

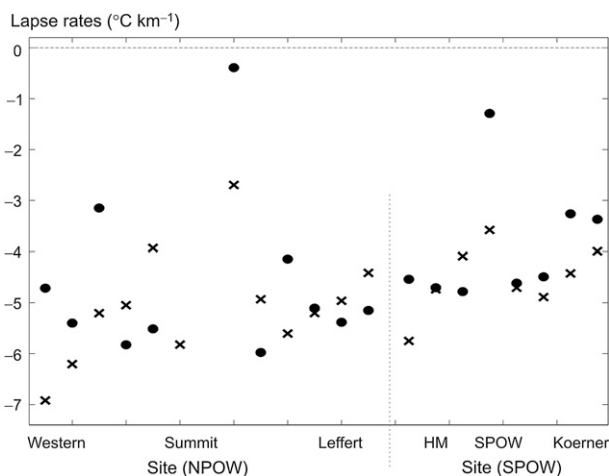


FIG. 10. Local lapse rates that are required to optimize temperature modeling over the ice field (2002/03 data), using the Summit site as the reference point on the ice field. Circles and crosses correspond to mean annual and summer lapse rates, respectively. The vertical dotted line separates NPOW vs SPOW sites.

The observations also offer numerous insights into downscaling and modeling of temperature fields for glacier mass balance modeling. Conventional free-air lapse rates of -6.5° to $-10^{\circ}\text{C km}^{-1}$ are steeper than observed near-surface temperature gradients on the ice field, leading to significant underestimation of summer melting on the ice field. Values of -4° to $-5^{\circ}\text{C km}^{-1}$ are recommended for melt modeling in this region and it may be fruitful to consider temporal (daily, monthly, seasonal, and interannual) variability of this parameter, providing one can unravel the synoptic controls of lapse rate variability at a specific site. The appropriate choice of lapse rate should be examined at any site where station data or modeled climate fields are being extrapolated or downscaled to an ice field for mass balance modeling.

In addition to temporal variability, there is systematic spatial variability in lapse rates associated with local or regional energy balance processes. Some of this structure could be parameterized for a region, given sufficient understanding of the near-surface energy balance conditions that govern local temperatures. This leads to a mass balance model that is far from parsimonious, with an unwieldy set of free parameters, but this is what may be demanded by the need for accurate local and regional temperature information. This applies to both temperature-index- and energy-balance-based melt models.

Other free parameters in degree-day melt models include measures of temperature variability, including both monthly and daily estimates of the standard deviation of temperature. Average annual values of σ_m and σ_d lead to overestimation of melt in the ice field ablation zone and are only appropriate at sites that are too cold to experience melting. Both measures vary spatially and temporally, but the first-order variability is driven by dampened fluctuations of air temperature over melting snow-ice in the summer melt season, when surface temperatures are pinned near 0°C . This effect can be captured by a simple sinusoidal seasonal cycle that prescribes reduced temperature variability over a melting glacier surface during the summer months. Alternatively, one of the reviewers suggests that σ_m and σ_d could be modeled as functions of the monthly and daily temperature; for example,

$$\sigma_m = \left\{ \begin{array}{l} \max[k(T_{\text{melt}} - \bar{T}_m), \sigma_m^{\text{max}}], \quad \bar{T}_m < 0^{\circ}\text{C} \\ \sigma_m^{\text{min}}, \quad \bar{T}_m \geq 0^{\circ}\text{C} \end{array} \right\}, \quad (7)$$

where $T_{\text{melt}} = 0^{\circ}\text{C}$ and k is a constant, tuneable with a dataset like that of this study. This is a useful suggestion because this approach to the parameterization is generally applicable to environments such as the tropics, where a sinusoidal annual temperature cycle is inap-

propriate, and to inland areas of the Greenland and Antarctic Ice Sheets, where temperatures remain well below melting. We have not tested this model but recommend it for future attempts to model the reduced temperature variability over melting snow-ice.

For the 2002/03 mass balance year, when we had good coverage of temperature and mass balance data over the POW Ice Field, monthly PDD melt models with a simple seasonal cycle for σ_m give the best fit to observed PDD and melt-day totals over the ice field. PDD modeling with a sinusoidal annual temperature cycle gave a weaker fit to the observations, particularly when average July temperatures were used to characterize the amplitude of the annual temperature cycle. Temperature from the warmest day of the year improved the model, but a sinusoidal annual cycle generally underestimates melting by giving only one episode per year of warm temperatures. In reality, synoptic weather variability can produce several such "melt episodes" over the ice field each summer. This result—poor characterization with a sinusoidal annual cycle—may be specific to polar ice fields, where summer melting is driven by a small number of synoptic events rather than a continuous melt season that lasts for several weeks or months.

We attain reasonable results in a simple model of ice field-wide mass balance based on our preferred PDD model and monthly temperature and precipitation data from the nearest available long-term weather station in Eureka, Nunavut. However, there are systematic discrepancies, particularly at the ice field margins, despite temperature and precipitation projections from Eureka that are specifically tailored for the POW Ice Field. Because the marginal ablation zones are the areas of greatest concern for ice field sensitivity to climate change, these results point to two major considerations for mass balance modeling of the high Arctic ice fields in northern Canada. Because of the complex geometry and scale of these ice fields and the strong influence of local/regional moisture sources, a physically based precipitation model is needed to capture precipitation gradients across the ice field. Second, energy balance processes at the ice field margins such as sensible heat advection (terrestrial margins) and local cloud cover (marine margins) cause systematic variations in temperature, making it difficult to apply a single lapse rate for temperature modeling across the ice field. Errors in the melt and mass balance modeling are dominated by errors in the temperature projections, and a successful mass balance model will likely need to embrace more sophisticated, physically based strategies (i.e., energy balance considerations) for temperature modeling. This is true for both energy balance and degree-day melt models.

Acknowledgments. We thank Canada's Polar Continental Shelf Project, Resolute Bay, Nunavut, for logistical support for the study. Additional support was provided by the Natural Sciences and Engineering Research Council (NSERC) of Canada and the Polar Climate Stability Network of the Canadian Foundation for Climate and Atmospheric Sciences (CFCAS). David Burgess, David Lewis, Douglas Mair, and Faron Anslow provided sterling field assistance for this study. Two anonymous reviews improved this contribution.

REFERENCES

- Arnold, N. S., I. C. Willis, M. J. Sharp, K. S. Richards, and M. J. Lawson, 1996: A distributed surface energy-balance model for a small valley glacier. I. Development and testing for Haut Glacier d'Arolla, Valais, Switzerland. *J. Glaciol.*, **42**, 77–89.
- Bøggild, C., N. Reeh, and H. Oerter, 1994: Modelling ablation and mass-balance sensitivity to climate change of Storstrømmen, northeast Greenland. *Global Planet. Change*, **9**, 79–90.
- Box, J. E., and Coauthors, 2006: Greenland ice sheet surface mass balance variability (1988–2004) from calibrated polar MM5 output. *J. Climate*, **19**, 2783–2800.
- Braithwaite, R. J., 1995: Positive degree-day factors for ablation on the Greenland ice sheet studied by energy-balance modelling. *J. Glaciol.*, **41**, 153–160.
- , and O. B. Olesen, 1989: Calculation of glacier ablation from air temperature, West Greenland. *Glacier Fluctuations and Climatic Change*, J. Oerlemans, Ed., Kluwer Academic, 219–233.
- , and Y. Zhang, 2000: Sensitivity of mass balance of five Swiss glaciers to temperature changes assessed by tuning a degree-day model. *J. Glaciol.*, **46**, 7–14.
- Cazorzi, F., and G. Dalla Fontana, 1996: Snowmelt modelling by combining temperature and a distributed radiation index. *J. Hydrol.*, **181**, 169–187.
- Cline, D. W., 1997: Snow surface energy exchanges and snowmelt at a continental, midlatitude Alpine site. *Water Resour. Res.*, **33**, 689–701.
- Fabre, A., C. Ritz, and G. Ramstein, 1996: Modelling of Last Glacial Maximum ice sheets using different accumulation parameterizations. *Ann. Glaciol.*, **24**, 223–229.
- Flowers, G. E., S. J. Marshall, H. Björnsson, and G. K. C. Clarke, 2005: Sensitivity of Vatnajökull ice cap hydrology and dynamics to climate warming over the next 2 centuries. *J. Geophys. Res.*, **110**, F02011, doi:10.1029/2004JF000200.
- Glover, R. W., 1999: Influence of spatial resolution and treatment of orography on GCM estimates of the surface mass balance of the Greenland Ice Sheet. *J. Climate*, **12**, 551–563.
- Hanna, E., P. Huybrechts, I. Janssens, J. Cappelen, K. Steffen, and A. Stephens, 2005: Runoff and mass balance of the Greenland Ice Sheet: 1958–2003. *J. Geophys. Res.*, **110**, D13108, doi:10.1029/2004JD005641.
- Hock, R., 1999: A distributed temperature-index ice- and snow-melt model including potential direct solar radiation. *J. Glaciol.*, **45**, 101–111.
- Huybrechts, P., 2002: Sea-level changes at the LGM from ice-dynamic reconstructions of the Greenland and Antarctic ice sheets during the glacial cycles. *Quat. Sci. Rev.*, **21**, 203–231.
- , A. Letréguilly, and N. Reeh, 1991: The Greenland ice sheet and greenhouse warming. *Global Planet. Change.*, **89**, 399–412.
- Jóhannesson, T., O. Sigurdsson, T. Laumann, and M. Kennett, 1995: Degree-day glacier mass-balance modelling with application to glaciers in Iceland, Norway, and Greenland. *J. Glaciol.*, **41**, 345–358.
- Koerner, R. M., 1979: Accumulation, ablation, and oxygen isotope variations on the Queen Elizabeth Islands ice caps, Canada. *J. Glaciol.*, **22**, 25–41.
- , 2002: Glaciers of the high Arctic islands. Satellite Image Atlas of Glaciers of the World: Glaciers of North America, U.S. Geological Survey Professional Paper 1386-J, R. S. Jr. and J. G. Ferrigno, Eds., J111–J146.
- Lefebvre, F., H. Gallée, J.-P. van Ypersele, and P. Huybrechts, 2002: Modelling of large-scale melt parameters with a regional climate model in south Greenland during the 1991 melt season. *Ann. Glaciol.*, **35**, 391–397.
- Letréguilly, A., N. Reeh, and P. Huybrechts, 1991: The Greenland Ice Sheet through the last glacial-interglacial cycle. *Global Planet. Change.*, **90**, 385–394.
- Marshall, S. J., M. J. Sharp, D. O. Burgess, and F. S. Anslow, 2007: Near-surface-temperature lapse rates on the Prince of Wales Icefield, Ellesmere Island, Canada: Implications for regional downscaling of temperature. *Int. J. Climatol.*, **27**, 385–398.
- Ohmura, A., 2001: Physical basis for the temperature-based melt-index method. *J. Appl. Meteor.*, **40**, 754–761.
- Pollard, D., and S. Thompson, 1997: Driving a high-resolution dynamic ice-sheet model with GCM climate: Ice-sheet initiation at 116,000 BP. *Ann. Glaciol.*, **25**, 296–304.
- Purves, R. S., and N. R. J. Hulton, 2000: A climatic-scale precipitation model compared with the UKCIP baseline climate. *Int. J. Climatol.*, **20**, 1809–1821.
- Radić, V., and R. Hock, 2006: Modelling future glacier mass balance and volume changes using ERA-40 and climate models: A sensitivity study at Storglaciären, Sweden. *J. Geophys. Res.*, **111**, F03003, doi:10.1029/2005JF000440.
- Reeh, N., 1991: Parameterization of melt rate and surface temperature on the Greenland Ice Sheet. *Polarforschung*, **59**, 113–128.
- Smith, R. B., and I. Barstad, 2004: A linear theory of orographic precipitation. *J. Atmos. Sci.*, **61**, 1377–1391.
- Wang, L., M. J. Sharp, B. Rivard, S. J. Marshall, and D. O. Burgess, 2005: Melt season duration on Canadian Arctic ice caps, 2000–2004. *Geophys. Res. Lett.*, **32**, L19502, doi:10.1029/2005GL023962.
- , M. Sharp, B. Rivard, and K. Steffen, 2007: Melt duration and ice layer formation on the Greenland ice sheet, 2000–2004. *J. Geophys. Res.*, **112**, F04013, doi:10.1029/2007JF000760.